

JGR Solid Earth

RESEARCH ARTICLE

10.1029/2020JB021098

Key Points:

- The total heat output is between 6.1 and 66 MW, making this vent field one of the most thermally significant in Yellowstone National Park
- Advection is the dominant mode of heat transport with a median (and 1σ range) of 29 (5.7–65) MW
- The median (and 1σ range) of conductive heat transport inside the vent field is 0.72 (0.33–1.4) MW

Supporting Information:

Supporting Information may be found in the online version of this article.

Correspondence to:

R. N. Harris,
rharris@ceoas.oregonstate.edu

Citation:

Favorito, J. E., Harris, R. N., Sohn, R. A., Hurwitz, S., & Luttrell, K. M. (2021). Heat flux from a vapor-dominated hydrothermal field beneath Yellowstone Lake. *Journal of Geophysical Research: Solid Earth*, 126, e2020JB021098. <https://doi.org/10.1029/2020JB021098>

Received 1 OCT 2020

Accepted 7 MAY 2021

Heat Flux From a Vapor-Dominated Hydrothermal Field Beneath Yellowstone Lake

Julia E. Favorito^{1,2}, Robert N. Harris¹ , Robert A. Sohn³ , Shaul Hurwitz⁴ , and Karen M. Luttrell⁵ 

¹College of Earth, Ocean, and Atmospheric Sciences, Oregon State University, Corvallis, OR, USA, ²Now at the Rivers School, Weston, MA, USA, ³Woods Hole Oceanographic Institution, Woods Hole, MA, USA, ⁴U.S. Geological Survey, Moffett Field, CA, USA, ⁵Department of Geology and Geophysics, Louisiana State University, Baton Rouge, LA, USA

Abstract We report results from 149 heat flux measurements made over an ~2-year interval at sites in and around a vapor-dominated geothermal field located at water depths of ~100–120 m in Yellowstone Lake, Wyoming. Measurements of both in situ temperature and thermal conductivity as a function of depth were made with a 1 m probe via a remotely operated vehicle, and are combined to compute the vertical conductive heat flux. Inside the $\sim 55.5 \times 10^3 \text{ m}^2$ bathymetric depression demarcating the vapor-dominated field, the median conductive flux is 13 W m^{-2} , with a conductive output of 0.72 MW. Outside the thermal field, the median conductive flux is 3.5 W m^{-2} . We observed 49 active vents inside the thermal field, with an estimated mass discharge rate of 56 kg s^{-1} , a median exit-fluid temperature of 132°C , and a total heat output of 29 MW. We find evidence for relatively weak secondary convection with a total output of 0.09 MW in thermal area lake floor sediments. Our data indicate that vapor beneath the thermal field is trapped by a low-permeability cap at a temperature of $\sim 189^\circ\text{C}$ and a depth of $\sim 15 \text{ m}$ below the lake floor. The thermal output of the Deep Hole is among the highest of any vapor-dominated field in Yellowstone, due in part to the high boiling temperatures associated with the elevated lake floor pressures.

1. Introduction

High enthalpy, vapor-dominated hydrothermal systems are characterized by locally elevated heat and gas fluxes. In these systems, steam and gases (mainly CO_2 and H_2S) ascend through the crust and accumulate beneath a low-permeability cap layer. Heat transfer through the cap causes the steam to condense, and the condensate descends, forming a two phase, vertical convective cell, often termed a “heat pipe” (White et al., 1971). The fluid dynamics and thermodynamics of vapor-dominated hydrothermal systems have been the subject of numerous field studies and modeling efforts (e.g., Allis, 2000; Hochstein & Bromley, 2005; Hurwitz et al., 2012; Ingebritsen & Sorey, 1988; McGuinness et al., 1993; Pruess, 1985; Pruess & Narasimhan, 1982; Scott, 2020; White et al., 1971). However, many key issues, such as the nature and extent of the low-permeability cap, the role of topographic relief, and the temporal evolution of the hydrothermal system, have yet to be resolved.

Vapor-dominated hydrothermal systems are ubiquitous in the Yellowstone National Park (YNP; Figure 1), where they are primarily manifested at the ground surface as mud pots and fumaroles (Bergfeld et al., 2012; Bouligand et al., 2019; Hurwitz & Lowenstern, 2014; Hurwitz et al., 2012; Lowenstern et al., 2012; Nordstrom et al., 2009; Werner et al., 2008; White et al., 1971; Zohdy et al., 1973). In these systems, which tend to be located at topographic highs, gas-rich (mainly CO_2 and H_2S) steam emissions produce acid-sulfate waters ($\text{pH} < 5$). In contrast, liquid-dominated systems produce alkaline-chloride fluids ($7 \leq \text{pH} \leq 10$) with little-to-no magmatic gases and tend to be located in lower elevation geyser basins. This dichotomy has been attributed to the position of the water table relative to the ground surface in the discharge zones (e.g., Hurwitz & Lowenstern, 2014). In lower elevation areas where liquid-dominated systems are prevalent, the water table is at, or just below the ground surface, which suppresses subsurface boiling. By contrast, at higher elevations where vapor-dominated systems are prevalent, the water table is assumed to be much deeper than the ground surface, allowing for the development of subsurface boiling zones, ascent of gas-rich vapor plumes, and the formation of clay-rich, low-permeability cap layers (Hurwitz et al., 2012; White et al., 1971).

This relatively simple topographic explanation, however, cannot account for the presence of vapor-dominated fields beneath the floor of the Yellowstone Lake (L. A. Morgan et al., 2003). The largest known such

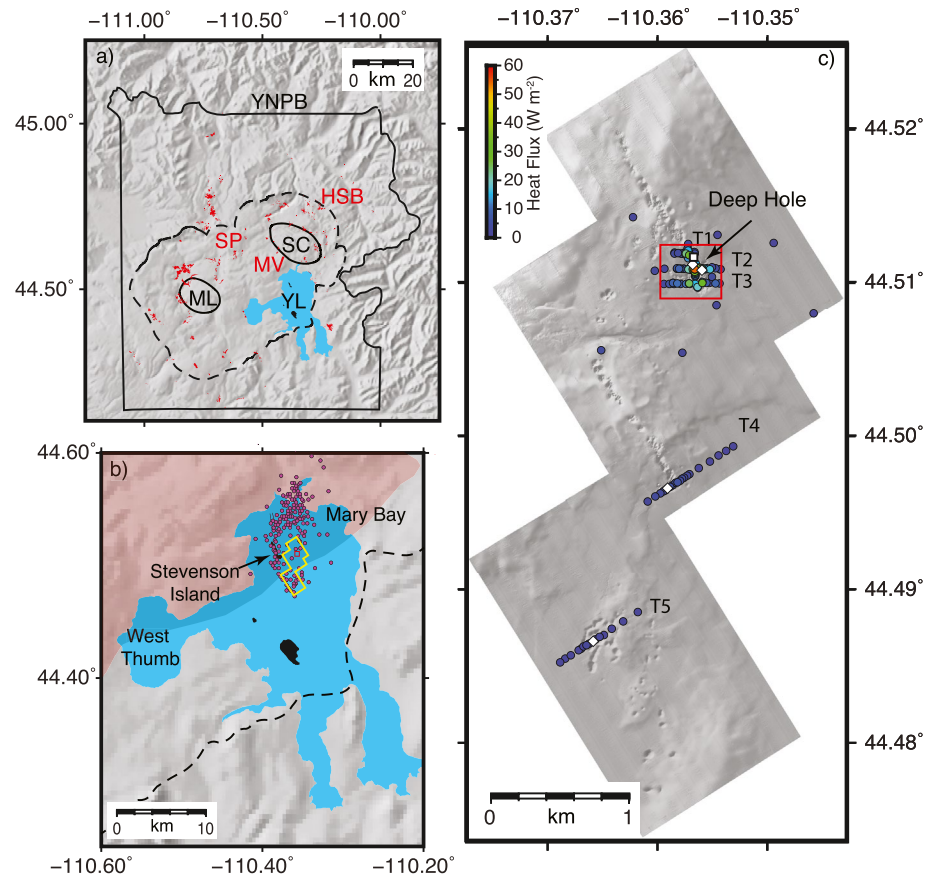


Figure 1. (a) Map of study area including Yellowstone National Park boundary (YNPB, black line), the 0.631-Ma caldera boundary (dashed line), Yellowstone Lake (YL), Sour Creek Dome (SC), and Mallard Lake Dome (ML). Geothermal areas are shown in red, including the vapor-dominated areas Mud Volcano (MV), Solfara Plateau (SP), and Hot Springs Basin (HSB). (b) Map of Yellowstone Lake (blue) and islands (black), with caldera boundary (dashed) and extent of high-resolution bathymetry shown in (c) (yellow). Magenta circles show epicenters of northward migration of 2008–2009 earthquake swarm (Farrell et al., 2010). Red shaded region shows surface projection of the Yellowstone magma reservoir (Farrell et al., 2014). (c) High-resolution bathymetry of the Deep Hole and surrounding region, with location of heat flux measurements (circles) colored by value. White diamonds show location of thermal gradient probes, and white square indicates Antares temperature probe used to monitor bottom water temperature variations (Supplemental Information S2). Heat flux transects are numbered from north to south. Most heat flux measurements were made along transects (T1–T5). Red box shows area of Figure 2.

field, informally known as the “Deep Hole” (e.g., Bouligand et al., 2020; Fowler, Tan, Cino, et al., 2019; R. A. Sohn et al., 2019; Tan et al., 2020), is located ~2 km southeast of Stevenson Island beneath more than 100 m of lake water (Figures 1 and 2). The Deep Hole field discharges hot (up to 174°C) fluids representing a mixture of vapor condensate, ambient lake water, and magmatic gases (dominantly CO₂ and H₂S) into the lake through a distributed set of active vents (Fowler, Tan, Cino, et al., 2019). The Deep Hole thermal area demonstrates that vapor-rich zones can form well below the local water table and that factors other than topography, such as permeability, can lead to the formation of vapor-dominated hydrothermal areas in Yellowstone.

Here we report the results of a multi-year heat flux survey conducted in and around the Deep Hole hydrothermal field. This work is part of a larger, multidisciplinary effort (Hydrothermal Dynamics of Yellowstone Lake, HD-YLAKE) aimed at understanding how lake floor hydrothermal systems respond to geological and environmental perturbations at multiple timescales (R. Sohn et al., 2017). The goals of this study are to quantify the heat and mass output of the Deep Hole, constrain the patterns and modes of hydrothermal circulation in the lacustrine sediments overlying the vapor reservoir, provide insight into the subsurface

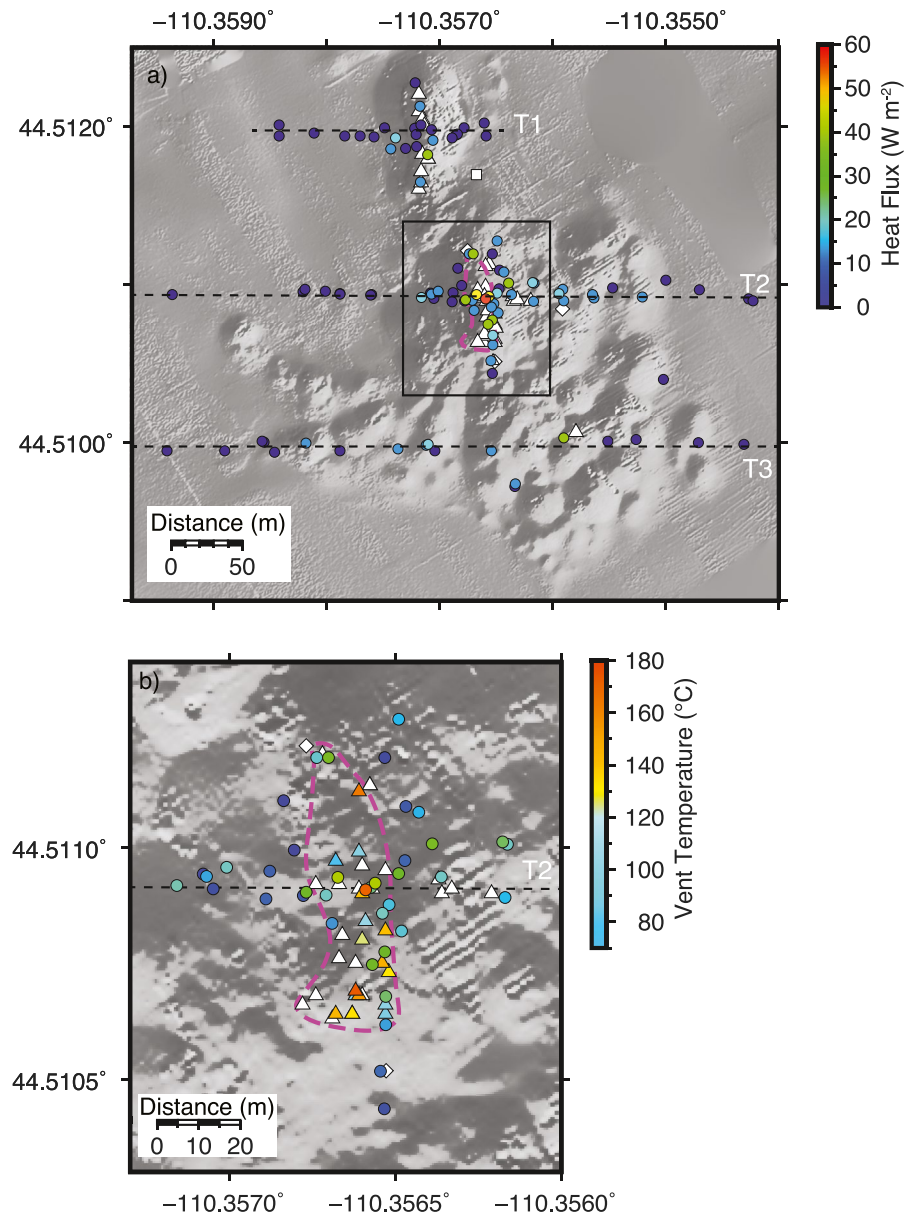


Figure 2. (a) Locations of heat flux measurement (circles colored by magnitude) and observed vents (white triangles, Table S1) in the Deep Hole. Transects, thermal gradient probes, and Antares temperature probe indicated by dashed black lines, white diamonds, and white square, respectively. Dashed magenta line encompasses the locus of verified active vents (Figure S7 and Table S1). Black box corresponds to area of panel (b). (b) Closeup of deepest and most active part of the Deep Hole, with vents (triangles) colored by vent fluid exit temperatures where available (Table S1).

processes and conditions that result in the formation of a vapor-dominated hydrothermal system beneath a deep (>100 m) lake, and place these results in the broader context of the Yellowstone hydrothermal system.

2. Geologic and Hydrothermal Setting

The $\sim 80 \times 50$ km Yellowstone Caldera was formed during the eruption of the 0.631 Ma Lava Creek Tuff (Christiansen, 2001; Christiansen et al., 2007). Seismic and strain data suggest that magma underlies much of the Yellowstone Caldera at depths ranging from 5 to 10 km and possibly shallower beneath portions of the eastern half of the caldera (Farrell et al., 2014; Luttrell et al., 2013). This magma is associated with a heat output of 4–8 GW (Hurwitz et al., 2012), abundant seismicity (e.g., Farrell et al., 2010), cycles of

ground surface uplift and subsidence (e.g., Chang et al., 2007; Dzurisin et al., 2012; Wicks et al., 2006), extensive CO₂ degassing (Hurwitz & Lowenstern, 2014; Werner & Brantley, 2003), and more than 10,000 hydrothermal features, including geysers, fumaroles, mud pots, and hot springs (Fournier, 1989; Hurwitz & Lowenstern, 2014; Lowenstern & Hurwitz, 2008). Nearly all of the thermal areas of the Yellowstone Plateau Volcanic Field are within the ~9,000 km² area of YNP (Figure 1a).

The northern part of the Yellowstone Lake occupies the southeastern portion of the Yellowstone Caldera (Figure 1). Following the eruption of the Lava Creek Tuff and collapse of the caldera, 600–1,000 km³ of rhyolitic lava flows were emplaced, within and along the caldera margins in multiple pulses. The lake was shaped by scouring from two major glaciations, the Bull Lake glaciation that peaked around 150 ka, and the Pinedale glaciation that began around 24 ka and receded from the Yellowstone Lake basin at about 14 ka (Licciardi & Pierce, 2018). Other dynamic processes shaping Yellowstone Lake include active fault systems, development of a series of postglacial shoreline terraces, and postglacial hydrothermal explosions, which created several craters (L. A. Morgan et al., 2003, 2009). The lake floor sediment is dominantly composed of diatomaceous (siliceous) ooze, ranging in thickness from <10 to ~100 m (Brown et al., 2019; Johnson et al., 2003; Otis et al., 1977).

Two heat flux campaigns have been previously carried out in Yellowstone Lake. P. Morgan et al. (1977) made 22 thermal gradient measurements at sites across all of the lake's major basins and arms. They acquired 5.8 m-long sediment cores at selected sites using a piston corer, yielding average bulk thermal conductivities of ~0.75 W m⁻¹ K⁻¹. This survey was later supplemented by a more comprehensive campaign that acquired 250 thermal gradient measurements (Blackwell et al., 1986). Both surveys used a 4.5 m, four thermistor, Bullard-type probe (Bullard, 1954). Outside the Yellowstone Caldera, heat flux varies between about 0.1 and 0.3 W m⁻², whereas at sites inside the caldera heat flux is generally higher and more variable with values between about 0.5 and 2 W m⁻², and individual measurements of up to 20 W m⁻² (Smith et al., 2009). Despite the wide spacing of these measurements (1–2 km), these studies demonstrated that heat flux is elevated inside the caldera, and identified heat flux anomalies in the West Thumb (1.6 W m⁻²), Mary Bay (15.6 W m⁻²), and the Deep Hole (5.0 W m⁻²) (Figure 1b). These anomalies are best explained by underlying advective heat transport (P. Morgan et al., 1977).

The Deep Hole hydrothermal field (Figure 2) is among the largest known active vent fields on the lake floor (R. A. Sohn et al., 2019). Bathymetric (L. A. Morgan et al., 2003), seismic reflection (Johnson et al., 2003), and magnetic (Bouligand et al., 2020; Finn & Morgan, 2002) data suggest that this feature is located near the southeast edge of a rhyolite flow (L. A. Morgan et al., 2003). The bathymetric depression is ~250 m wide and as deep as ~40 m below the surrounding lake floor and is narrower and steeper to the north, and broader to the south. The depression was likely formed by a combination of sediment expulsion and dissolution due to hydrothermal discharge (Shanks et al., 2005). Within the Deep Hole, bathymetry is relatively rough, having relief that manifests as a region of overlapping and superimposed pockmarks. Individual pockmarks have typical diameters of ~10–60 m and depths of 5–10 m. At the Deep Hole, existing seismic reflection data does not resolve the composition and thickness of the substrate, but lacustrine sediments outside of the Deep Hole are at least 20 m thick (Johnson et al., 2003).

Vent fluid samples from the Deep Hole indicate a vapor reservoir at relatively shallow depths beneath the local lake floor (Fowler, Tan, Cino, et al., 2019; Fowler, Tan, Luttrell, et al., 2019). The chemical (high CO₂ and H₂S, low Cl relative to lake water) and isotopic (δ D and δ^{18} O) compositions of these vent fluids are consistent with binary mixing of a condensed vapor and lake water. In the conceptual model presented by Fowler, Tan, Cino, et al. (2019), vapor escapes the reservoir at discrete locations, condenses upon encountering cooler lake sediments and/or mixing with colder pore fluids, and the condensate buoyantly rises through the shallow sediments, discharging into the lake. An enthalpy balance calculation indicates that the vent fluids consist of ~19–22 wt% condensed steam and ~78–81 wt% lake water (Fowler, Tan, Cino, et al., 2019).

3. Conceptual Model of the Deep Hole Hydrothermal System

Several studies have defined the main features of subaerial vapor-dominated systems in YNP (e.g., Bouligand et al., 2019; Hurwitz et al., 2012; White et al., 1971). Meteoric water percolates deep in the subsurface where it is heated by rock surrounding the underlying magma. Hot, upwelling fluids encounter low-permeability

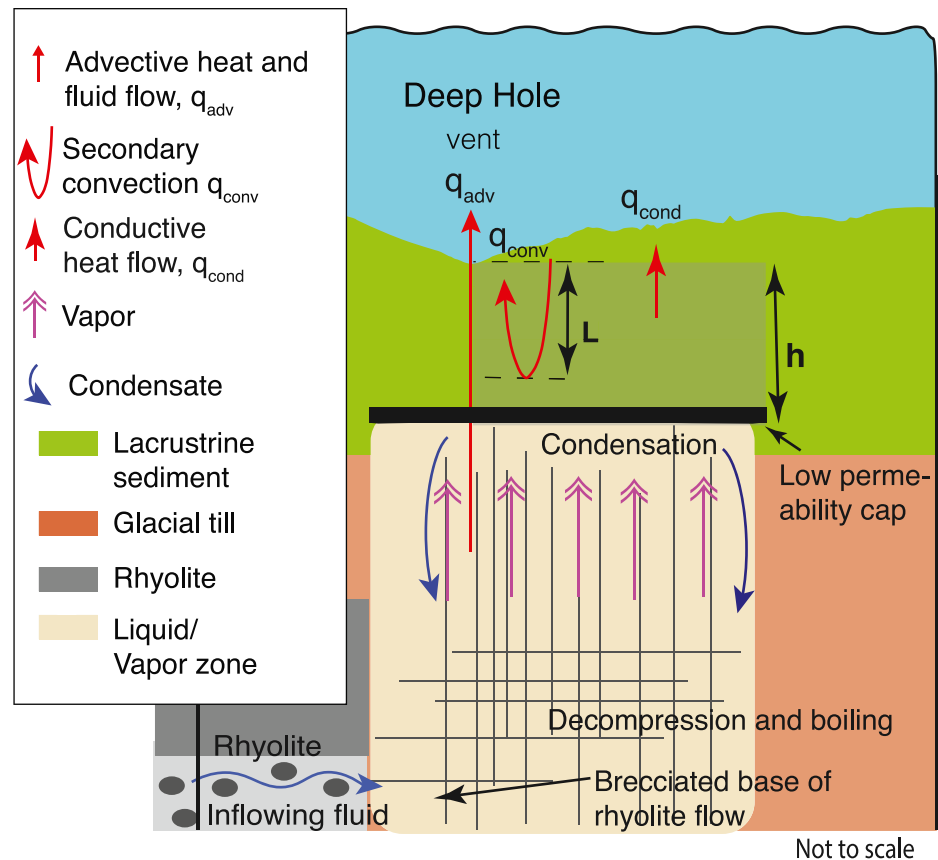


Figure 3. Conceptual model (not to scale) of the vapor-dominated system at the Deep Hole southeast of Stevenson Island. At depth, heat is transported by lateral groundwater flow at the base of a rhyolite flow. The breccia provides a higher permeability conduit. At the rhyolite flow termination, groundwater is discharged into glacial deposits of lower permeability, decompresses, and boils. The vapor, rises in a network of fractures, condenses at the base of a low-permeability cap, and flows down driven by gravity (“heat pipe”). Heat is conductively transported across the low-permeability cap, except where a fracture transects the cap material (depicted by long red arrow). Lake water and condensate mix in the sediments and fracture above the low-permeability cap. Permeability increases in near surface lake sediments allowing recirculation (convection) of lake water. Although we do not know the lithology at the base of the low-permeability cap, we place it near the lacustrine sediment-glacial till interface. Shaded region shows the model domain (Figure 7) for heat conduction simulations. L is the scale length of convective flow in upper sediments and h is the depth to the base of the low-permeability cap, relative to the maximum lake floor depth.

lava flows, migrate laterally to flow edges, and resume their ascent through higher permeability glacial sediments, where they decompress and vaporize (Hurwitz & Lowenstern, 2014; L. A. Morgan et al., 2009). The buoyant, multiphase (liquid and steam) fluid rises, likely through a high permeability network of fractures, until it is arrested by a clay-rich, low-permeability cap (Bouligand et al., 2019; Hurwitz et al., 2012). Conductive heat transfer through the cap condenses vapor, and the heavier condensate descends in an annulus around the vapor-rich zone, forming a narrow convection cell (“heat pipe,” White et al., 1971). Where fractures penetrate the low-permeability cap, some of the steam and gas are emitted to the atmosphere through fumaroles (Bouligand et al., 2019; Hurwitz & Lowenstern, 2014).

This model requires some modifications in order to apply it to the sublacustrine Deep Hole hydrothermal field (Figure 3). Whereas the ambient ground surface pressure in subaerial settings is atmospheric, at the Deep Hole the lake floor underlies ≥ 100 m of water, which significantly increases the saturation (boiling) temperature. In addition, because the water table is much higher than the lake floor, a low-permeability cap is likely needed to protect the steam reservoir from being flooded with groundwater, and allows for the possibility of secondary convection of pore fluids in the sediments overlying the cap.

4. Methods

We acquired heat flux data from the Deep Hole and the surrounding area over three consecutive field seasons during August 2016, 2017, and 2018 (Figure 1). During the first field season, 36 heat flux measurements were made in and around the Deep Hole. During the second field season, 34 heat flux measurements were made on transects crossing pockmark fields to the south of the Deep Hole, and 22 were made in and around the Deep Hole. All 57 measurements in the third field season were focused in and around the Deep Hole. In total, we made 149 new heat flux measurements during the field campaign.

Heat flux measurements were made from the research vessel (R/V) *Annie II* using the remotely operated vehicle (ROV) *Yogi*, both owned and operated by the Global Foundation of Ocean Exploration. Data were acquired using a 1 m-long probe designed and maintained by the National Deep-Submergence Facility at the Woods Hole Oceanographic Institution. The probe contains five thermistors that are spaced 20 cm apart and calibrated to an accuracy of 0.01°C. The probe is capable of determining both the in situ temperature gradient and sediment thermal conductivity. During deployment, the probe was mounted to the ROV frame and inserted into the sediment using the downward propulsion of the ROV. Navigation of the ROV, and therefore the thermal measurements, is accurate to ± 2.5 m horizontally. Probe tilt was monitored using the ROV pitch and roll. Relative to vertical the tilt is generally less than 1°.

Equilibrium temperatures and the thermal conductivities at each thermistor were determined using a modified version of the method described by Villinger and Davis (1987) as implemented by Stein and Fisher (2001) and described in the Supporting Information S1. Heat flux was computed as the slope relating temperature to summed thermal resistance (supporting information, Equation S1; Figure S1), which accounts for variations in thermal conductivity (Bullard, 1939). We quantified thermal perturbations associated with bottom water temperature variations (0.1% of the mean background thermal gradient of 4.5°C m⁻¹, Supporting Information S2) and sedimentation rate (less than ~1% of mean background thermal gradient, Supporting Information S3) and corrected for bathymetry that on average decreases heat flux by about 7% (Supporting Information S4). Bottom water temperature variations and sedimentation rates have a relatively small effect in part because the thermal gradients are relatively large.

Measurements of thermal gradient are accurate to about 1% and thermal conductivity measurements are accurate to about 5% (Nagihara & Lister, 1993) so that the heat flux determinations are accurate to about 6% (Bevington & Robinson, 1992). We estimate that the accuracy of the bathymetric correction is about 5%. The propagation of uncertainties suggest our bathymetrically corrected heat flux values are accurate to about 10%.

Vent exit-fluid temperatures were measured with a titanium-sheathed temperature probe during the first two field seasons (Fowler, Tan, Cino, et al., 2019; Fowler, Tan, Luttrell, et al., 2019). We estimated the effective radius (vent orifices are not perfectly circular) of some vents using parallel red lasers (10 cm spacing) mounted on the ROV and/or by comparison with vent fluid sampling instruments of known size.

5. Results

Heat flux measurements are focused along five transects oriented to cross the major thermal features; three of which cross the Deep Hole, and two cross pockmark fields south of the Deep Hole (Figure 1). Transects 1, 2, and 3, cross the northern, central, and southern portions of the Deep Hole (Figure 2), respectively. Because temperature gradient measurements made at the same location during different field seasons do not show resolvable differences, we assume that thermal conditions are at a quasi-steady state and combine the data from all three field seasons in the following analyses.

Of the 149 heat flux locations, in situ thermal conductivity was measured at 103 sites (as described in Supporting Information S1) and estimated from nearby measurements at 46 sites. The bulk thermal conductivity (sediment and fluid) at sites inside and outside (including the southern transects) the Deep Hole are 0.94 ± 0.22 ($n = 41$) and 0.89 ± 0.06 W m⁻¹ K⁻¹ ($n = 62$), respectively. Figure 4 shows histograms of heat flux data inside and outside of the Deep Hole. Sites within the Deep Hole have a median value of 13 W m⁻² and a 1 σ range from 5.9 to 25 W m⁻². Values outside the Deep Hole have a median value of 3.5 W m⁻² and a 1 σ

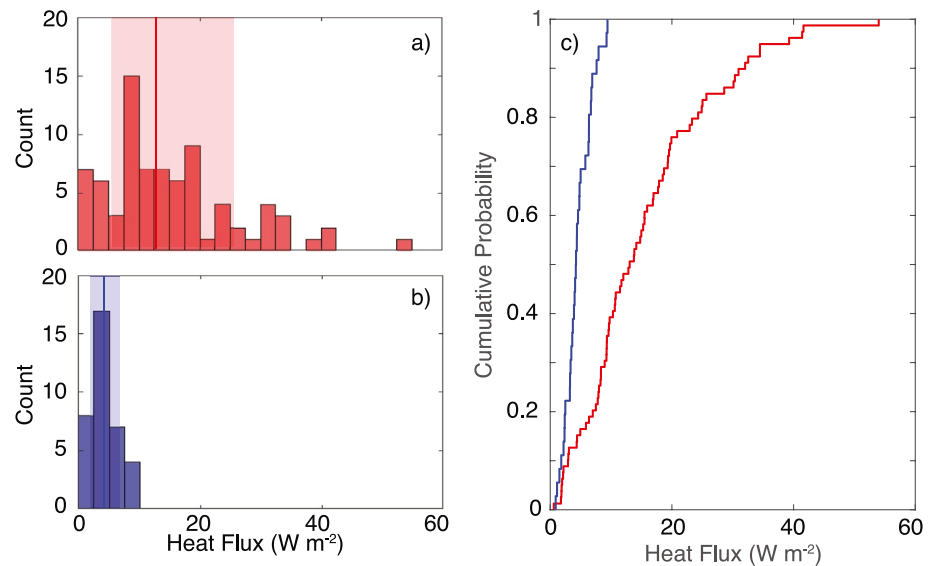


Figure 4. Distributions of heat flux data. (a) Histogram of heat flux values inside the Deep Hole. The solid vertical line shows the median value, and the shaded areas show the range containing one standard deviation of the data. (b) Histogram of heat flux values outside the Deep Hole. Solid vertical line and shading as in panel (a). (c) Cumulative distributions of the heat flux data. Data acquired inside the Deep Hole thermal area are shown in red, and data acquired outside the thermal area are shown in blue.

range from 1.4 to 5.1 W m⁻². A two-sample Kolmogorov-Smirnov test indicates that these two populations are statistically different at the 95% confidence interval.

Heat flux values outside of the Deep Hole are relatively uniform whereas those inside the Deep Hole are considerably higher and more variable (Figure 5). The highest heat flux values are in close proximity to active vents (Figure 2b) and approach 55 W m⁻² as shown on Transect 2 (Figure 5b). Overall, the high heat flux values (≥ 30 W m⁻², $n = 11$) delineate an approximately linear trend that is aligned with the trend of active vents (Figure 2b). Heat flux decreases south of the Deep Hole (Transects 4 and 5 in Figure 5) with a median value of 1.9 W m⁻² and a 1σ range of 1.4–4.0 W m⁻². This median heat flux value is similar to the mean heat flux through Yellowstone Caldera of 2.3 W m⁻² (Hurwitz et al., 2012) and represents the regional, intracaldera, background value.

At the lake floor, visual observations of vents during ROV surveys of the Deep Hole indicate that they present as irregular features in the weakly consolidated soft sediment that forms the lake floor. In contrast to submarine hydrothermal vents, these sublascustrine vents are destructional rather than constructional in nature, and create localized depressions in the sediments surrounding the discharge zones. As a result of sediment removal due to hydrothermal discharge, vents are found in the deepest parts of the thermal field, at water depths ranging from 105 to 112 m, with a mean depth of 109 m below the present lake surface (lake water level varies annually by ~ 1 –2 m). Forty-nine hydrothermal vents were identified (Supplementary Information, Table S1) of which 31 are confirmed as active through visual observations of shimmering water. The remaining 18 vents were identified during flyovers by the ROV but were not confirmed active due to poor visibility but are deemed likely active. In some cases, high heat flux values (> 26 W m⁻²) near these vents attest to their activity (Figure 2). Measurement of vent fluid temperatures range from 74°C to 173°C, with a median value of 132°C (Figure 2b). The upper limit of the temperature measurements (173°C) corresponds to the saturation temperature at in situ pressure (Tan et al., 2017). Vent radii range between 0.5 and 9.4 cm with a median radius of 2.5 cm and 1σ range of 1.9–3.8 cm (Supporting Information S5).

Figure 6 shows heat flux values as a function of distance from the closest mapped vent. Heat flux values between $\sim 1,200$ and 1,600 m from the closest vent correspond to Transect 4 and values between $\sim 2,400$ and 2,900 m correspond to Transect 5. Heat flux values are largest close to vents and both the magnitude and scatter decrease with distance from mapped vents. However, some of the lowest values are close to mapped vents, suggesting there is downward pore fluid flow at these sites, likely associated with recharge of

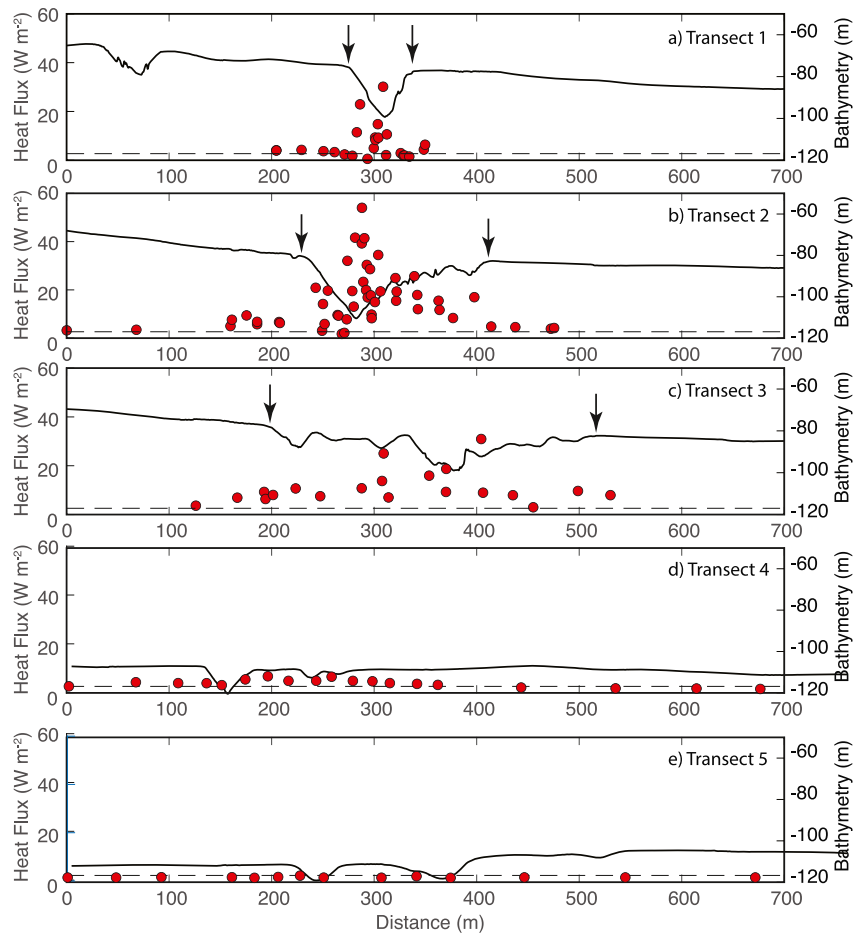


Figure 5. Transects showing heat flux measurements (red circles) and bathymetry relative to lake level (solid line). Transect locations are shown in Figure 1c. Transects 1–3 cross the Deep Hole thermal field (panels a–c), with vertical arrows marking the edges of the pockmarks that demarcate the thermal field, which grow wider from north to south. Transects 4 and 5 (d and e) cross individual pockmark trends located to the south of the Deep Hole. Heat flux determination uncertainty is $\sim 10\%$. The regional background heat flux ($\sim 2 \text{ W m}^{-2}$) is shown as a dashed black line in all panels.

a shallow convection system, as we discuss in Section 6.2. Overall, we find that the primary factor influencing heat flux values within the Deep Hole is proximity to active vents.

6. Heat Transport Models

There are three primary heat transport mechanisms associated with the Deep Hole field: conduction and convection through the sediment overlying the vapor reservoir, and advection through vents (Figure 3). Here, we focus on Transect 2 that crosses the most active vent field within the Deep Hole (Figure 2b), where we have good spatial coverage of both heat flux and vent exit-fluid temperatures. The heat flux data allow us to estimate the magnitude of the conductive component, a parametric analysis allows us to estimate the magnitude of pore fluid convection, and vent exit-fluid temperatures and effective radii measurements allow us to estimate the magnitude of the advective component. Below, we describe these models, and the resulting heat output estimates.

6.1. Conductive Heat Transport Model

Given the roughly linear alignment of the active venting sites within the Deep Hole and the fact that heat flux is primarily determined by proximity to an active vent, we conceptualize conductive heat flux from the

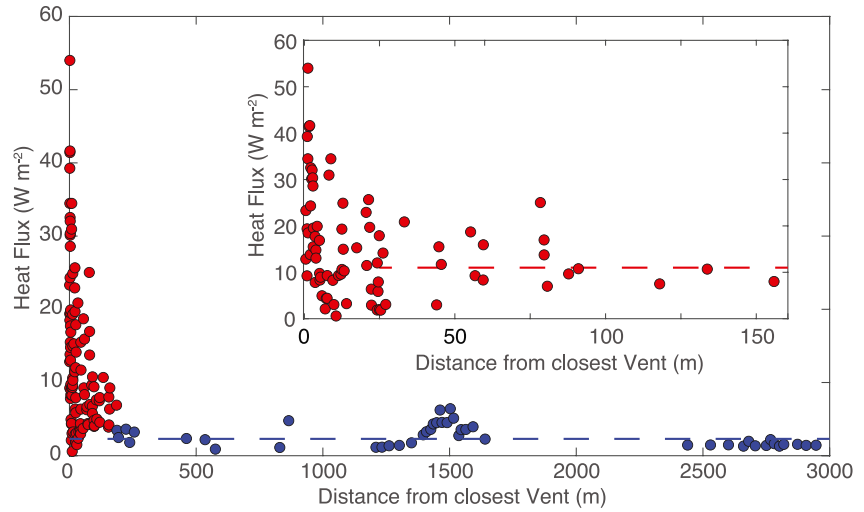


Figure 6. Heat flux values as a function of distance from closest active vent. Red circles show measurements within the Deep Hole and blue circles show measurements outside the Deep Hole. Blue-dashed horizontal line shows estimated intracaldera heat flux of 2.3 W m^{-2} (Fournier, 1989). Inset shows expanded view of values inside the Deep Hole and red dashed horizontal line shows median heat flux within the Deep Hole of 13 W m^{-2} .

sediments above the vapor reservoir as being symmetric about an infinitely long, vertical plane representing a crack or fissure containing hydrothermal fluids. We construct a two-dimensional model domain consisting of liquid water-saturated porous sediments with a uniform bulk thermal conductivity of $0.9 \text{ W m}^{-1} \text{ K}^{-1}$. The top of the model represents the lake floor, and the bottom of the model represents the base of the low-permeability cap layer (i.e., the top of the vapor reservoir), at a depth, h , below the lake floor (Figures 3 and 7). The left side of the model domain represents the hot, fluid filled fracture containing hydrothermal fluids, and the right side of the model ($w = 150 \text{ m}$) represents background thermal conditions (i.e., sediments that are far enough away from active vents such that their temperature is not affected by lateral diffusion of heat from hot fluids). We assume a flat upper boundary because we removed the effects of lake bottom relief on the heat flux data with a bathymetric correction (Supporting Information S4), and a flat lower boundary for simplicity because data supporting lateral variations in the depth to the vapor reservoir are not available.

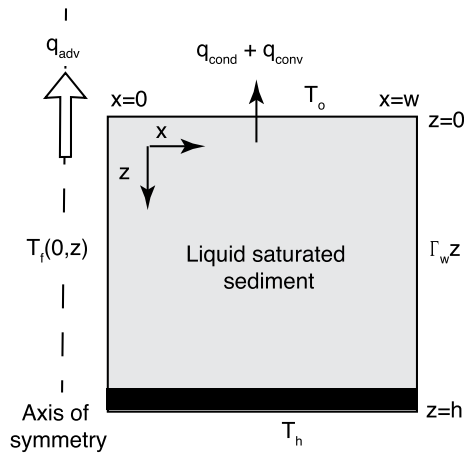


Figure 7. Schematic representation of the finite difference model domain containing liquid water saturated sediments with a bulk thermal conductivity (solid + water) of $0.9 \text{ W m}^{-1} \text{ K}^{-1}$. The finite difference model is applied to quantify conductive (q_{cond}) heat transport. Convective (q_{conv}) and advective (q_{adv}) heat transport (conceptually shown in Figure 3) are calculated using other methods. Black bar shows low-permeability cap. Symbols defining the boundary conditions are described in Table 1.

We use a finite difference scheme to solve the two-dimensional steady state heat flux equation,

$$\frac{\partial^2 T}{\partial x^2} + \frac{\partial^2 T}{\partial z^2} = 0 \quad (1)$$

within the model domain, where T is temperature, x and z are horizontal and vertical coordinates, respectively, subject to the following boundary conditions,

$$T(x, 0) = T_o$$

$$T(0, z) = T_f(z)$$

$$T(w, z) = T_o + \Gamma_w z$$

$$T(x > 0, h) = T_h$$

where T_o is the mean bottom water temperature of 4°C , Γ_w is the background thermal gradient within the thermal area, and $T_f(z)$ is the

Table 1
Symbol Definitions

Parameter	Meaning	Units
A	Area of the Deep Hole	m^2
c_f	Fluid specific heat	$\text{J kg}^{-1} \text{K}^{-1}$
f	Friction factor	Dimensionless
g	Acceleration of gravity	m s^{-2}
H	Enthalpy	kJ kg^{-1}
h	Depth to base of low-permeability cap	m
k	Permeability	m^2
L	Flow path length	m
L_p	Length of probe	m
M_v	Vapor mass condensation rate	kg s^{-1}
Pe	Peclet number	Dimensionless
Q_{cond}	Conductive heat output	W
Q_{conv}	Convective heat output	W
Q_{adv}	Advective heat output	W
Δq	Heat flux difference	W m^{-2}
q_o	Surface heat flux	W m^{-2}
q_{cond}	Conductive heat flux	W m^{-2}
q_{conv}	Convective heat flux	W m^{-2}
q_{adv}	Advective heat flux	W m^{-2}
q_b	Background heat flux	W m^{-2}
q_m	Median heat flux	W m^{-2}
q_{model}	Model heat flux	W m^{-2}
Ra	Rayleigh number	Dimensionless
Re	Reynolds number	Dimensionless
r	Vent radius	m
T	Temperature	$^{\circ}\text{C}$
T_o	Bottom water temperature	$^{\circ}\text{C}$
T_h	Temperature at depth h	$^{\circ}\text{C}$
$T_f(z)$	Fracture geotherm	$^{\circ}\text{C}$
ΔT	Temperature difference	K
v_z	Vertical velocity	m yr^{-1}
w	Width of finite difference domain	m
x	Horizontal coordinate	m
z	Vertical coordinate	m
α	Thermal diffusivity	$\text{m}^2 \text{s}^{-1}$
β	Coefficient of thermal expansion	K^{-1}
ϵ	Relative roughness	Dimensionless
ϕ	Porosity	Dimensionless
Γ	Thermal gradient	K m^{-1}
Γ_w	Far field thermal gradient	K m^{-1}
λ	Thermal conductivity	$\text{W m}^{-1} \text{K}^{-1}$
ν	Kinematic viscosity	$\text{m}^2 \text{s}^{-1}$

geotherm (vertical temperature profile) within the fracture (i.e., temperature on the left side of the model domain). We use a constant temperature basal boundary condition, T_h , at depth h , representing the temperature of saturation (condensation) at the appropriate pressure. Definitions and values of symbols are given in Table 1. We assume that vapor condensation occurs at $z > h$ (below the base of the low-permeability cap layer), and that there is no heat generation within the model domain. Below, we estimate values for these boundary conditions.

We estimate the depth to the top of the vapor reservoir, h , by assuming this is the depth, where the background geotherm intersects the boiling curve for pure water. The representative far-field thermal gradient due to conduction through the sediments overlying the vapor reservoir is given by $\Gamma_w = q_b/\lambda$, where q_b is the background heat flux in the Deep Hole, and λ is the effective sediment thermal conductivity ($0.9 \text{ W m}^{-1} \text{ K}^{-1}$). We estimate the background heat flux by taking the median value of the heat flux observations within the Deep Hole after removing observations made within the mapped vent field (Figure 2). Although empirical, these values must be removed because hydrothermal fluids ascending through discrete fractures generate a thermal halo that increases heat flux in the surrounding sediments above the background value. The median value of heat flux measurements that are not affected by active discharge is $q_b = 11 \text{ W m}^{-2}$ with a 1σ range of $5.7\text{--}22 \text{ W m}^{-2}$. This background flux estimate yields a representative conductive thermal gradient, Γ_w , of $12^{\circ}\text{C m}^{-1}$.

With a hydrostatic load of 109 m corresponding to the mean depth of active vents, the geotherm intersects the boiling curve for pure water at a depth, h , of $\sim 15 \text{ m}$ below the lake floor, at a saturation temperature of 189°C , consistent with estimates based on chemical geothermometry and the relations between in situ sampling temperature, and dissolved CO_2 concentration in the Deep Hole fluid samples (Fowler, Tan, Luttrell, et al., 2019). We also computed the boiling curve for a $\text{H}_2\text{O-CO}_2$ fluid based on a CO_2 concentration of 20 mmol/kg (Fowler, Tan, Luttrell, et al., 2019; Hurwitz et al., 2016), but the difference is negligible ($<1 \text{ m}$, $\sim 0.5^{\circ}\text{C}$). Boiling curves are calculated as in Hurwitz et al. (2016) using data from National Institutes of Standards and Technology (<http://webbook.nist.gov/chemistry/fluid>) database. These values set the depth and temperature at the base of the model.

The temperature-depth profile in the vertical fracture, $T_f(z)$, is constrained at the top by hydrothermal fluid temperature measurements made in the Deep Hole vents (median value of 132°C , Fowler, Tan, Cino, et al., 2019; Fowler, Tan, Luttrell, et al., 2019; Tan et al., 2020, Table S1), and at the bottom by the saturation temperature corresponding to the ambient pressure at the top of the vapor reservoir (189°C). The range of possible conditions is thus constrained by two end-member, isothermal scenarios, corresponding to $T_f = 132^{\circ}\text{C}$ and $T_f = 189^{\circ}\text{C}$. We ran the model using these two isothermal scenarios for the fracture boundary conditions, and found that the difference in surface heat flux resulting from the two end-member geotherms is small (Figure 8).

Our conductive heat flux model captures the first order spatial trends observed in our data, with values being highest near the fracture, and decaying quickly away from the fracture to values of $\sim 10\%$ of the maximum at a lateral offset distance equal to h . This indicates that, to first-order,

Table 1
Continued

Parameter	Meaning	Units
ρ_v	Density, water vapor	kg m^{-3}
ρ_f	Fluid density	kg m^{-3}

variations in conductive heat flux can be understood as being due to the lateral diffusion of heat from a hot, fluid-filled fracture, superimposed on a background vertical flux from a buried vapor reservoir. To check that our results are not unduly influenced by bathymetric variations, we also ran models where the lake floor interface followed the local bathymetry (rather than a flat interface), but the resulting thermal gradients were not significantly different in the upper meter of the sediments, where our data were acquired, demonstrating that bathymetric variations have only a small effect on conductive heat flux in the thermal field.

There is a considerable degree of variability in our heat flux measurements, and in particular, we observe values well below the background value of 11 W m^{-2} at short offset distances from the fracture (Figures 5 and 6). These anomalously low heat flux observations suggest that secondary porous convection within the Deep Hole sediments may be generating recharge zones that depress the local thermal gradient, and thus heat flux, consistent with inferences from time-series vertical temperature profiles acquired in the Deep Hole (Sohn & Harris, 2021).

6.2. Secondary Convection Within the Upper Sediments

The presence of a hot interface ($\sim 189^\circ\text{C}$ at the top of the vapor reservoir) at a relatively shallow depth beneath the lake floor and a vertical crack containing hot hydrothermal fluids have the potential to stimulate convection of sediment pore fluids. Any such convection would create warm discharge zones and cold recharge zones (Figure 3). We assess the possibility of porous convection using a Rayleigh number criterion, and consider whether or not it could explain the observed variability in our heat flux measurements.

The Rayleigh number, Ra , for groundwater flow in lake sediments above the low-permeability cap can be expressed as (Nield, 1968),

$$Ra = \frac{g\beta kh\Delta T}{v\alpha} \quad (2)$$

where g is the acceleration of gravity (9.8 m s^{-2}), β is the coefficient of thermal expansion of water ($4.09 \times 10^{-4} \text{ K}^{-1}$), k is permeability (m^2), ΔT is the temperature difference between lake water (4°C) and the base of the vapor reservoir (189°C), v is the kinematic viscosity of water ($3.18 \times 10^{-7} \text{ m}^2 \text{ s}^{-1}$), and α is the bulk thermal diffusivity ($1.67 \times 10^{-7} \text{ m}^2 \text{ s}^{-1}$). Assuming that a critical Rayleigh number of ~ 10 is required to stimulate convection in a porous medium with a fixed upper temperature and a basal heat flux (Nield, 1968), we find that convection could occur if the sediment permeability is greater than $\sim 5 \times 10^{-14} \text{ m}^2$. Permeabilities of siliciclastic material and diatoms that characterize the unaltered lake floor sediments can be greater than $5 \times 10^{-14} \text{ m}^2$ (Bryant & Rack, 1990; Spinelli et al., 2004), while permeabilities of hydrothermally altered sediments rich in clay, quartz, and pyrite can be significantly lower (Dobson et al., 2003). We thus find that heat transport by secondary convection is plausible within unaltered lacustrine sediments, but unlikely within highly altered sediments, such as those comprising the low-permeability cap overlying the vapor reservoir.

Before estimating the vertical fluid flow, velocities needed to account for the misfit between the measured heat flux values, and those calculated with the conductive heat transport model (Figure 8), we place an upper limit on the vertical flow velocity based on the observation that our temperature-thermal resistance profiles used to estimate conductive flux do not show systematic curvature (supporting information, Figures S1–S2). Vertical pore fluid flow above some threshold velocity would add curvature to these profiles, and the degree of curvature depends on the Peclet number (Pe), the ratio of advective to conductive heat transport, expressed as,

$$Pe = \phi v_z \rho_w c_w L_p / \lambda \quad (3)$$

where ϕ is porosity, λ is the effective thermal conductivity ($0.9 \text{ W m}^{-1} \text{ K}^{-1}$), ρ_w is the water density, c_w is the specific heat of water, L_p is a vertical length scale (here equal to the length of the heat flux probe, 1 m), and v_z

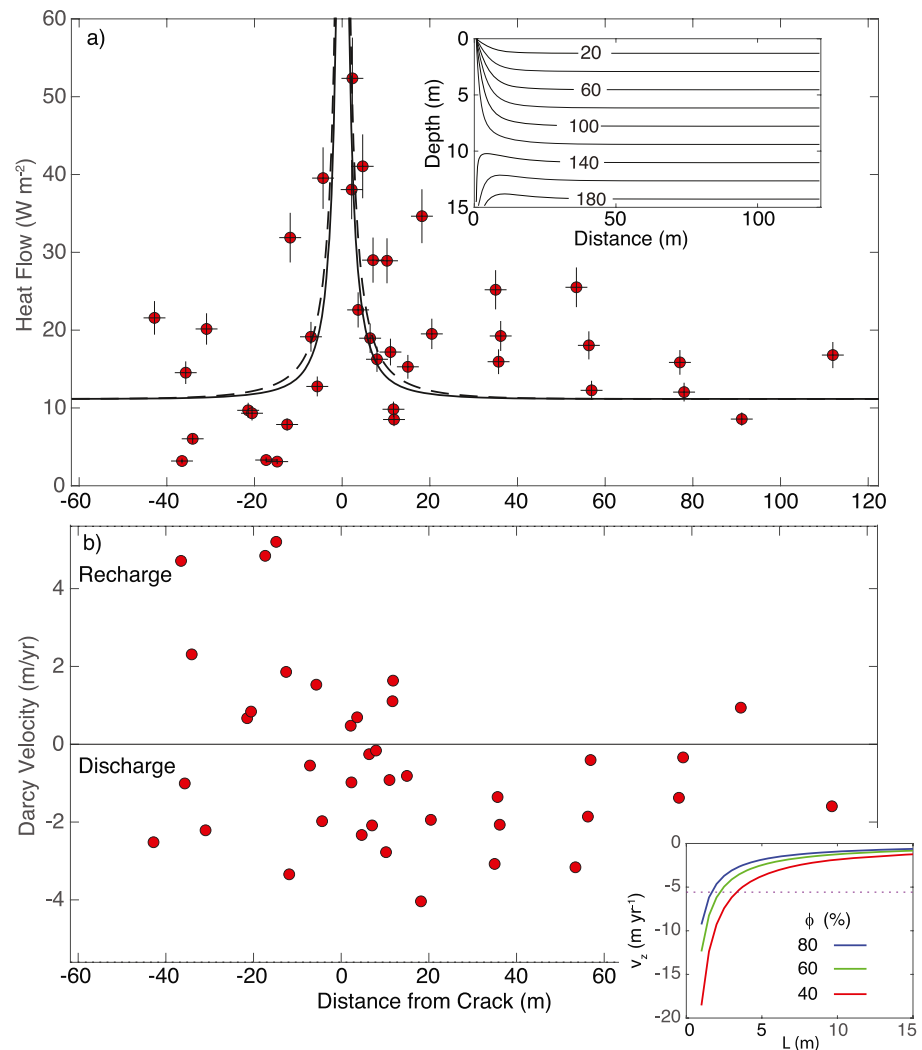


Figure 8. (a) Comparison of measured heat flux values along Transect 2 inside the Deep Hole with model results. Red circles show measured heat flux values with estimated uncertainties. Black solid, and dashed lines show model results for a geotherm in the fracture ($x = 0$), corresponding to median vent exit-fluid temperature (132°C), and the reservoir temperature (189°C), respectively. Inset shows results of the thermal model with an isothermal fracture at 132°C. Contours are isotherms in °C. Model depth is set to bottom of cap layer, $(h)/h$. (b) Vertical groundwater velocity at each measurement location estimated assuming that the misfit between measured and calculated heat flux values are due to vertical pore fluid flow. Positive values correspond to discharge from the sediment and negative values correspond to recharge into the sediment. The limits of the vertical axis are set to the groundwater vertical velocity threshold required to generate observable curvature in the thermal resistance plots (Figure SI-2). Inset shows mean vertical velocity, v_z , as a function of path length, L , for three different porosity values.

is the mean vertical groundwater velocity. Porosity values in the top 1 m of sediments in the range between 60% and 96%, and we use the mean of about 80% (Tiller, 1995) for our calculations.

The threshold Peclet number for generating detectable curvature in a temperature-thermal resistance profile is 0.5 (Bredehoeft & Papadopoulos, 1965), and under the parameterization described above this corresponds to a curvature of 1.5 K W⁻¹ in temperature-thermal resistance profiles and a vertical groundwater velocity of 5.6 m yr⁻¹. Since all of our temperature-thermal resistance profiles have curvatures less than 1.5 K W⁻¹, we take 5.6 m yr⁻¹ as an upper limit on the possible vertical velocity of pore fluids in the Deep Hole sediments.

We estimate the pore fluid vertical velocities required to explain the misfit between our conductive heat flux model and our heat flux measurements using a one-dimensional model of steady-state groundwater flow in porous media,

$$\frac{\partial^2 T}{\partial z^2} - \frac{\phi \rho_w c_w}{\lambda} v_z \frac{\partial T}{\partial z} = 0 \quad (4)$$

For boundary conditions, we assume an isothermal lake floor, and that the thermal gradient at depth L is given by the thermal model. The difference between the measured and modeled heat flux can be expressed as (Lubimova et al., 1965)

$$v(L) = -\frac{\lambda}{\phi \rho_w c_w L} \ln \left(\frac{q_{obs}}{q_{model}} \right) \quad (5)$$

Here, the vertical groundwater velocity required to explain the model misfit is a function of the total flow path length, L . Given that pore fluid convection is unlikely within the altered sediments that comprise the low-permeability cap overlying the vapor reservoir, the maximum value of L corresponds to the depth of the top of this cap, which is unknown, but is constrained to be less than 15 m (top of the vapor reservoir) and greater than 3 m (in order to not exceed the threshold velocity). We estimate the minimum value of L using the maximum misfit between the observed data and the background value in the heat transport model (22 W m^{-2} , Figure 8b, inset). The minimum value of L that accounts for this misfit and does not exceed the threshold velocity is 3 m. For each heat flux measurement shown in Figure 8a, we use Equation 5 to compute the vertical fluid velocity required to adjust it to match the expected model value for conductive heat transport at that distance from the model fracture (Section 6.1). Estimated groundwater velocity values with a path length of 3 m are shown in Figure 8b and indicate a mean vertical water velocity of -0.6 m yr^{-1} , suggesting that along Transect 2, discharge is greater than recharge. If instead, we take the maximum path length L of 15 m (such that secondary circulation reaches the bottom of the low-permeability cap layer), the estimated mean vertical velocity is -0.1 m yr^{-1} . These values lead to Peclet numbers between 0.17 and 0.06 and an estimate of convective heat flux of between 0.78 and 2.2 W m^{-2} . When integrated over the area of the Deep Hole, this corresponds to a total secondary convective heat output of $\sim 0.09 \text{ MW}$.

6.3. Advective Heat Transport Through Vents

The advective discharge of hot hydrothermal fluid occurs through a discrete set of vents positioned along a roughly linear trend (Figure 2). While conceptualizing hydrothermal upflow as occurring within a linear, vertical fracture is reasonable for modeling conductive heat flux, it would substantially overestimate the advective flux since the observed discharge zones constitute only a small fraction of the linear distance along the axis of the Deep Hole (supplemental information Section S6). To account for this, we conceptualize advective flux as occurring through a discrete set of vertical pipes located along a linear trend, rather than along an entire linear flow channel.

The advective heat, Q_{adv} , through an individual vertical pipe is given by,

$$Q_{adv} = \rho_f c_f \pi r^2 v_z \Delta T \quad (6)$$

where ρ_f and c_f are the density and specific heat of the vent fluid, r is the effective pipe radius, and ΔT is the temperature difference between the vent fluid and ambient bottom water. We were unable to obtain direct estimates of fluid flow rates through the vents, so we estimate this parameter following the approach of Strens and Cann (1986), which balances the buoyancy force of hot ascending fluid against frictional resistance. In this model, the vertical fluid velocity is expressed as,

$$v_z = \left[\frac{2g(\rho_f - \rho_v) r}{(\rho_f + \rho_v) f} \right]^{\frac{1}{2}} \quad (7)$$

where ρ_f and ρ_v are the mean densities of the ambient bottom water (4°C) and vent fluids, respectively (neglecting salinity effects), and f is the pipe friction factor. A key unknown is the variation of pipe (vent) radii with depth in the sediments. We therefore assume that the surface measurements of vent radii can be extended to the entire vertical length in the sediment. The friction factor, f , is calculated based on the flow Reynolds number, Re , and the relative roughness of the pipe walls, ϵ (Colebrook, 1939),

$$\frac{1}{\sqrt{f}} = -2 \log_{10} \left(\frac{2.51}{Re \sqrt{f}} + \frac{\epsilon}{3.7} \right) \quad (8)$$

For reasonable values of fluid velocity <10 m/s (Ramondenc et al., 2006; Sarrazin et al., 2009) and the observed range of vent radii, the Reynolds number is on the order of $\sim 1 \times 10^5$, which is in the turbulent flow regime, implying that f is relatively insensitive to the first term in the parentheses of Equation 8. Because video images of active vents show occlusions, we increase the relative roughness, ϵ , of 0.05 (Strens & Cann, 1986) by a factor of 10, which yields a friction factor of ~ 0.06 . With this value and a median effective vent radius of 2.5 ± 2 cm, Equation 7 yields a median vertical flow velocity of 0.6 ± 0.2 m s⁻¹.

Based on a total of 49 active vents, a median vent exit-fluid temperature of 132°C, a median effective vent radius of (2.5 cm), and a vent exit-fluid velocity of 0.6 m s⁻¹, Equation 6 yields a median advective heat output of 29 MW. Because the parameters used in Equation 6 are not normally distributed, we use a Monte Carlo analysis that uses bootstrap replicates of the parameters to estimate uncertainty (Robens, 2021). Based on this analysis, we calculate an advective heat output between 5.7 and 65 MW. Substituting Equation 7 into Equation 6 shows that the advective heat output depends on $r^{5/2}$, and the large uncertainty in the advective heat output estimate is due to the large range in vent radii. These parameters yield a (median) total mass discharge rate of 56 kg s⁻¹.

7. Discussion

We conducted a detailed heat flux survey of the Deep Hole, a sublacustrine, vapor-dominated hydrothermal system southeast of Stevenson Island in Yellowstone Lake. We measured heat flux during three consecutive summers from 2016 to 2018 at 149 sites, 115 of which were inside or on the perimeter of the Deep Hole.

The mean value of thermal conductivity for the shallow sediments sampled in our study is 0.9 W m⁻¹ K⁻¹, consistent with the highly porous ($\sim 80\%$, Tiller, 1995) sediments that comprise the upper meter of the lake bed, and is similar to the average value of 0.75 W m⁻¹ K⁻¹ reported by P. Morgan et al. (1977). The mean value of thermal conductivity is slightly higher, and the scatter is larger inside the Deep Hole compared with its surroundings. This is consistent with the results of Sohn & Harris (2021), who found higher sediment thermal diffusivity values for sites inside the Deep Hole relative to those outside. These differences are likely due to the effects of hydrothermal alteration. Sediments outside the Deep Hole are siliceous ooze dominantly composed of diatoms (i.e., amorphous silica/opal), with minor amounts of potassium feldspar, clays (smectite), and quartz (Shanks et al., 2007; Tiller, 1995). In contrast, sediments near active vents in the Deep Hole are highly altered and contain 80–99 wt% kaolinite with minor boehmite, pyrite, quartz, and smectite (Fowler, Tan, Luttrell, et al., 2019).

The total heat output from the Deep Hole ranges between 6.1 and 66 MW with a preferred value of 30 MW (Table 2). When distributed over the entire area of the Deep Hole, we obtain an average heat flux estimate ranging between 111 and 1163 W m⁻².

There are several heat transport mechanisms inside the thermal area: advection, conduction, and secondary convection. Our analysis indicates that advective transport is at least one and possibly two orders of magnitude greater than conductive transport, and at least two and possibly three orders of magnitude greater than convective transport. Advection is the dominant heat transport mechanism, even after considering the wide

Table 2
Calculated Medians and 1σ Range (in Parentheses) for Heat Output of the Deep Hole

Q_{cond} MW	Q_{conv} MW	Q_{adv} MW	Q_{total} MW	Area m^2	q_{total} W m^{-2}
0.72 (0.33–1.4)	0.09 (0.04–0.12)	29 (5.7–65)	30 (6.1–66)	$\sim 55.5 \times 10^3$	540 (110–1,189)

Q_{cond} is the conductive heat output. Q_{conv} is heat output of secondary convection. Q_{adv} is the advective heat output. Q_{total} is the total heat output. q_{total} is the total heat flux.

range of possible values (5.7–65 MW). As noted previously, our advective flux estimates are highly sensitive to the vent radii (i.e., cross-sectional areas), which are difficult to measure, and our assumption of vertical pipes with constant radii is almost certainly an over-simplification. Upflow paths are likely tortuous, and to the extent that they occur in “pipes,” there are likely variations in the pipe radius along the flow path. In addition, our advective estimate is based on discharge from 49 vents that were visually identified or sampled during ROV dives, and this value represents a minimum since it is unlikely that we detected all of the active vents. Nevertheless, our advective flux estimate agrees well with that of R. A. Sohn et al. (2019), who estimated an advective heat output of 28 MW (possible range of 20–45 MW) from the Deep Hole based on the neutral buoyancy height of the water column plume generated by hydrothermal discharge (~ 70 m above the local lake floor). The consistency between the two estimates is noteworthy because they are derived from independent sets of observations and models, indicating that our advective flux estimate is likely first-order accurate despite all of the inherent uncertainties.

The complete set of conductive heat flux measurements made inside the Deep Hole have a median value of 13 W m^{-2} and a 1σ range from 5.9 to 25 W m^{-2} . Values within the mapped vent field (Figure 2) have a larger median value of 24 W m^{-2} and a 1σ range of $13\text{--}54 \text{ W m}^{-2}$, reflecting the impact of lateral heat diffusion from zones of hot, ascending fluids (Figure 8). In general, elevated sediment temperatures and heat flux values extend to ~ 20 m from active upflow zones. Outside of the Deep Hole heat flux has a median value of 2.3 W m^{-2} and 1σ range of $1.4\text{--}5.1 \text{ W m}^{-2}$. These values overlap with the estimated 2.3 W m^{-2} average heat flux of the Yellowstone Caldera (Fournier, 1989; Hurwitz et al., 2012). Our analysis assumes a steady heat flux over the two-year time interval of our survey such that we could group measurements acquired over three consecutive field seasons into a single data set. However, given the observed spatial heterogeneity and the ROV navigational uncertainties (within 5 m), any temporal changes in heat flux would need to have been of large magnitude and spatial extent to have been unequivocally detected. Thermal gradient time-series data acquired during the field campaign indicate that there are temporal variations in heat flux across the lake-sediment interface due to changes in bottom water temperature. The magnitude of these variations relative to the background flux, however, is small (Supporting Information S2). Two time-series records of vertical temperature profile were acquired inside the Deep Hole from August, 2017 to ,2018 (Sohn & Harris, 2021). One of these, but not the other, exhibited a systematic decrease of $\sim 10^\circ\text{C/m}$ over a ~ 6 -month interval that is not related to lake bottom water temperature variations. This temperature decrease was interpreted to result from a local redistribution of heat due to changing fluid flow paths through the sediments (e.g., Sohn, 2007) rather than a system-wide fluctuation. In this scenario, the total advective heat output of the thermal area is essentially constant but the location of the vertical pipes hosting advective flux and the strength of the flux in any given pipe can change over time due to the effects of hydrothermal flow (e.g., alteration, sediment expulsion).

Estimates of secondary convection within the lacustrine sediments overlying the low-permeability cap were deemed reasonable based on a Rayleigh number calculation and considerations of lake sediment permeability. These estimates rely on the difference between the observed values of heat flux along Transect 2 and the results of the conductive heat transport model. When assessing these results it is important to recall that we parameterized the hydrothermal upflow as being continuous along a linear trend. In reality, the upflow zone consists of discrete vents distributed within a zone with an approximately linear trend, and this could cause spatial variations in sediment temperatures that add misfit to the model. Nevertheless, taking the misfits at face value, we find that any such convection must penetrate at least 3 m into the sediments in order to match our observation and not generate detectable curvature in temperature-thermal resistance profiles. If the convection cells have aspect ratios of ~ 1 , then a high-degree of short wavelength (~ 3 m) variability would be expected for heat flux measurements, consistent with our observations (Figure 8a). Overall,

Table 3
Heat Flux From Vapor-Dominated Areas in and Around Yellowstone National Park

Area	Heat Output MW	Area km ²	Heat flux W m ⁻²
Deep Hole ^a	6.1–66	0.06	110–1,200
Obsidian pool thermal area ^b	11.8 ± 1.4	0.11	103 ± 2
Solfatara Plateau thermal area ^b	8.8 ± 0.4	0.25	35 ± 3
Mud Volcano thermal area ^c	30.4	0.4	76
Hot Spring Basin ^d	140–370	1.0	140–370
Yellowstone Plateau volcanic field ^b	4,000–8,000	2,435	2.3

^aThis study. ^bHurwitz et al. (2012). ^cChiodini et al., (2005). ^dWerner et al. (2008).

our analysis indicates that while secondary convection can locally modify thermal gradients and conductive heat flux, the total heat output of convection (0.09 MW) is negligible compared to that from advection or conduction.

The background conductive heat flux within the Deep Hole is ~5x larger than the intracaldera average, underscoring the impact of the vapor reservoir on the local thermal environment. If the elevated background level of conductive heat flux inside the Deep Hole (11 W m⁻²) relative to the intracaldera background level (2.3 W m⁻², Hurwitz et al., 2012), is entirely due to the flux of latent heat released by condensation, the vapor mass condensation rate, M_v , can be expressed as,

$$M_v = \Delta q * A / H \quad (9)$$

where $\Delta q = 11 - 2.3 = 8.7$ W m⁻², A is the surface area of the Deep Hole (55.5 × 10³ m²), and H is the latent heat of condensation (1,985 kJ kg⁻¹). Equation 9 yields a vapor mass condensation rate of 0.2 kg s⁻¹. This value is considerably smaller than the total condensate discharge rate through

vents, which is estimated to be ~11 kg s⁻¹ (assuming condensate represents 20% of the total fluid mass, Fowler, Tan, Cino, et al., 2019).

The total heat flux through the Deep Hole (111–1168 W m⁻²) is among the highest of any vapor-dominated thermal areas in YNP (Table 3). The high flux is at least partly due to the large difference between saturation versus ambient temperatures at the lake floor. In Yellowstone's subaerial systems, the difference between the saturation temperature (~92°C) and the mean annual air temperature (1°C) at the ground surface is about half that of the Deep Hole system (saturation ~173°C, bottom water ~4°C). In a sense, measuring the heat flux at the lake floor is analogous to making measurements at deep interfaces in subaerial systems, which illustrates how the lake floor provides a window into the hydrothermal systems that is generally unavailable in subaerial systems. Although heat flux in the Deep Hole is more intense than its subaerial counterparts, the total heat output is similar due to the relatively small size of the lake floor field (Table 3).

Of the three linear pockmark trends delineating sites of past or present hydrothermal discharge in our study area (Figure 1), we only detected active discharge along the northernmost trend where the Deep Hole is located. However, heat flux values crossing the middle pockmark trend along Transect 4 are locally elevated, suggesting that remnant heat from the active phase of those vents is still being dissipated conductively. In contrast, heat flux values from the southernmost pockmark trend crossed by Transect 5 are uniformly low, indicating that any thermal perturbations associated with active venting have completely dissipated. Overall, heat flux values within our study area thus increase to the north, reaching maximum values within the active venting zone of the Deep Hole. This overall trend is consistent with previous heat flux surveys (Blackwell et al., 1986; P. Morgan et al., 1977) and proximity to the surface projection of the magma reservoir.

The 2008–2009 Yellowstone Lake earthquake swarm (Farrell et al., 2010), which has been interpreted as being driven by migrating hydrothermal fluids, originated almost directly beneath our Transect 5 (Figure 1) and migrated due north, passing beneath all of the other transects before stopping near the lake's northern shore. Because the swarm occurred almost a decade before our heat flux surveys (Farrell et al., 2010; Massin et al., 2013), we are unable to assess its impact on heat flux. However, our results demonstrate that heat flux progressively increases to the north along the swarm migration path within our survey area. We did not make any observations to the north of the Deep Hole field, but submersible observations have documented a hydrothermally altered dome ~2.5 km north of the Deep Hole (L. A. Morgan et al., 2009), which is also aligned with the swarm migration path. This dome (informally known as the Northern Dome) stands ~30 m above the surrounding lake floor and contains numerous hydrothermal features, including active discharge at temperatures of up to 100°C, microbial mats, and highly altered sediments. Taken together, these observations are consistent with the propagation path of the 2008–2009 swarm representing a hydrothermal belt, where fluids ascend to the ground surface in discrete zones that are progressively migrating northwards. This temporal evolution may provide a means to study the processes and timescales by which

vent fields are initiated and abandoned in the lacustrine environment and suggests that new sites may be initiated to the north of the Northern Dome in the future.

Our results represent the first detailed heat flow survey of a sublacustrine hydrothermal field, and they raise interesting questions. The largest sources of uncertainty in our study were the effective radius (cross-sectional area) of the upflow zones in the sediments, and the vertical velocity of the hot fluids in these flow pipes. Techniques capable of better constraining these parameters would significantly improve our understanding of sublacustrine heat flow, and reduce the uncertainty of the advective heat flow estimates. More generally, the temporal evolution of thermal fields on the lake floor remains poorly understood, and the apparent relationship between the northward migration of hydrothermal discharge zones and the 2008–2009 earthquake swarm migration path warrants a more comprehensive treatment than that provided here.

8. Conclusions

Our high spatial-resolution heat flux data from the Deep Hole thermal field provide new insights into the mechanisms and rates of heat transport in sublacustrine vapor-dominated hydrothermal systems environments, and lead us to the following conclusions:

1. The total heat output (and 1σ range) of the Deep Hole is 30 (6.1–66) MW, of which 29 (5.7–65) MW is due to advection through the hydrothermal vents, 0.72 (0.33–1.4) MW is due to conduction, and 0.09 (0.04–0.12) MW is due to convection in shallow lake sediments. The large uncertainty in the estimates of advective heat output is primarily due to uncertainties in the cross-sectional area of the vents and vertical flow velocities.
2. Heat flux from the Deep Hole is between 110 and 1,200 W m⁻², significantly greater than the average heat flux from the Yellowstone Caldera and from the intra-caldera portion of Yellowstone Lake. Heat flux from the Deep Hole is more intense than those from any other subaerial vapor-dominated field in Yellowstone with the possible exception of Hot Springs Basin (Werner et al., 2008).
3. The median (and 1σ range) of conductive heat flux inside versus outside the Deep Hole is 13 (5.9–25) W m⁻² versus 3.5 (1.4–5.1) W m⁻², respectively. Secondary convection in shallow lake sediments can explain the misfit between measured and modeled conductive flux estimates, but the net heat output by secondary convection is negligible.
4. The Deep Hole field is underlain by a vapor reservoir that is capped by a low-permeability feature at a depth of ~15 m below to the lake floor. The saturation temperature at this interface is ~189°C. The vapor reservoir is capped by low-permeability rocks, likely formed by hydrothermal alteration of silica-rich sediments to clays.
5. The total mass flux rate through active vents in the Deep Hole is ~56 kg s⁻¹, of which ~11 kg s⁻¹ is condensed vapor (~20%), and the remainder is entrained lake water. If the difference in conductive heat flux inside versus outside the thermal area is due to the latent heat released by condensation, the vapor condensation rate beneath the low-permeability cap is ~0.2 kg s⁻¹.

Acknowledgments

The authors thank Yellowstone National Park Fisheries and Aquatic Sciences, the Global Foundation for Ocean Exploration, and the Woods Hole Oceanographic Institution Deep Submergence Laboratory for logistical support. They appreciate comments from J. Vandemeulebrouck, E. Burns, M. Clynne, an anonymous reviewer, and the associate editor that helped improve this study. This work was funded by U.S. National Science Foundation (NSF) grants EAR-1515283 to R. N. Harris and J. E. Favorito, EAR-1516361 to R. A. Sohn, and EAR-1514865 to K. M. Luttrell. All work in Yellowstone National Park was completed under research permit (YELL-2018-SCI-7018) and the authors thank Annie Carlson from the Yellowstone Center for Resources for logistical help.

Data Availability Statement

The heat flux and bathymetry data reported in this paper are available through the Marine Geoscience Data System (<http://doi.org/10.26022/IEDA/329828> and <http://doi.org/10.26022/IEDA/329678>). Any use of trade, firm, or product names is for descriptive purposes only and does not imply endorsement by the U.S. Government.

References

- Allis, R. (2000). Insights on the formation of vapor-dominated geothermal systems. *Proceedings World Geothermal Congress 2000, Kyushu-Tohoku, Japan, May 28-June 10, 2000*. Japanese Organizing Committee for WGC 2000.
- Bergfeld, D., Evans, W. C., Lowenstern, J. B., & Hurwitz, S. (2012). Carbon dioxide and hydrogen sulfide degassing and cryptic thermal input to Brimstone Basin, Yellowstone National Park, Wyoming. *Chemical Geology*, 330–331, 233–243. <https://doi.org/10.1016/j.chemgeo.2012.09.001>
- Beverington, P. R., & Robinson, D. K. (1992). *Data reduction and error analysis for the physical sciences*. New York: McGraw-Hill.
- Blackwell, D. D., Morgan, P., Spafford, R., & Steele, J. (1986). Heat flow from Yellowstone Lake, Yellowstone Caldera, Wyoming. *Eos: Transactions of the American Geophysical Union*, 67, 1226.

- Bouligand, C., Hurwitz, S., Vandemeulebrouck, J., Byrdina, S., Kass, M. A., & Lewicki, J. L. (2019). Heat and mass transport in a vapor-dominated hydrothermal area in Yellowstone National Park, USA: Inferences from magnetic, electrical, electromagnetic, sub-surface temperature, and diffuse CO₂ flux measurements. *Journal of Geophysical Research: Solid Earth*, *124*, 291–309. <https://doi.org/10.1029/2018JB016202>
- Bouligand, C., Tivey, M. A., Finn, C. A., Morgan, L. A., Shanks, W. C. P., III, & Sohn, R. A. (2020). Geological and thermal control of the hydrothermal system in Northern Yellowstone Lake: Inferences from high-resolution magnetic surveys. *Journal of Geophysical Research: Solid Earth*, *125*, e2020JB019743. <https://doi.org/10.1029/2020JB019743>
- Bredehoeft, J. D., & Papaopulos, I. S. (1965). Rates of vertical groundwater movement estimated from the Earth's thermal profile. *Water Resource Research*, *1*, 325–328. <https://doi.org/10.1029/WR001i002p00325>
- Brown, S. R., Fritz, S. C., Morgan, L. A., & Shanks, W. C., III. (2019). Fossilized diatoms of siliceous hydrothermal deposits in Yellowstone National Park, USA. *Diatom Research*, *34*, 193–204. <https://doi.org/10.1080/0269249X.2019.1698466>
- Bryant, W. R., & Rack, F. R. (1990). Consolidation characteristics of Weddell Sea sediments: Results of ODP Leg 113. In P. F. Barker, & J. P. Kennet (Eds.), *Proceedings of the ocean drilling program, scientific results* (pp. 211–223). College Station, TX: Ocean Drilling Program. <https://doi.org/10.2973/odp.proc.sr.113.173.1990>
- Bullard, E. C. (1939). Heat flow in South Africa. *Proceedings of the Royal Society of London*, *A173*, 474–502. <http://doi.org/10.1098/rspa.1939.0159>
- Bullard, E. C. (1954). The flow of heat through the floor of the Atlantic Ocean. *Proceedings of the Royal Society of London, Series A, Mathematical and Physical Sciences*, *222*, 408–429. <https://doi.org/10.1098/rspa.1954.0085>
- Chang, W.-L., Smith, R. B., Wicks, C., Farrell, J. M., & Puskas, C. M. (2007). Accelerated uplift and magmatic intrusion of the Yellowstone Caldera, 2004 to 2006. *Science*, *318*, 952–956. <https://doi.org/10.1126/science.1146842>
- Chiodini, G., Granieri, D., Avino, R., Caliro, S., Costa, A., & Werner, C. (2005). Carbon dioxide diffuse degassing and estimation of heat release from volcanic and hydrothermal systems. *Journal of Geophysical Research*, *110*, B08204. <https://doi.org/10.1029/2004JB003542>
- Christiansen, R. L. (2001). *The Quaternary and Pliocene Yellowstone Plateau volcanic field of Wyoming, Idaho, and Montana*. U.S. Geological Survey. <https://doi.org/10.3133/pp729G>
- Christiansen, R. L., Lowenstern, J. B., Smith, R. B., Heasler, H., Morgan, L. A., Nathenson, M., et al. (2007). *Preliminary assessment of volcanic and hydrothermal hazards in Yellowstone National Park and vicinity*. U.S. Geological Survey. Retrieved from <https://pubs.usgs.gov/of/2007/1071/>
- Colebrook, C. F. (1939). Turbulent flow in pipes, with particular reference to the transition region between the smooth and rough pipe laws. *Journal of the Institution of Civil Engineers*, *11*, 133–156. <https://doi.org/10.1680/jjoti.1939.14509>
- Dobson, P. F., Kneafsey, T. J., Hulén, J., & Simmons, A. (2003). Porosity, permeability, and fluid flow in the Yellowstone geothermal system, Wyoming. *Journal of Volcanology and Geothermal Research*, *123*(3–4), 313–324. [https://doi.org/10.1016/S0377-0273\(03\)00039-8](https://doi.org/10.1016/S0377-0273(03)00039-8)
- Dzurisin, D., Wicks, C., & Poland, M. P. (2012). *History of surface displacements at the Yellowstone Caldera, Wyoming, from leveling surveys and InSAR observations, 1923–2008* (p. 68). U. S. Geological Survey Professional Paper. Retrieved from <https://pubs.usgs.gov/pp/1788/>
- Farrell, J., Smith, R. B., Husen, S., & Diehl, T. (2014). Tomography from 26 years of seismicity revealing that the spatial extent of the Yellowstone crustal magma reservoir extends well beyond the Yellowstone Caldera. *Geophysical Research Letters*, *41*, 3068–3073. <https://doi.org/10.1002/2014GL059588>
- Farrell, J., Smith, R. B., Taira, T., Chang, W.-L., & Puskas, C. M. (2010). Dynamics and rapid migration of the energetic 2008–2009 Yellowstone Lake earthquake swarm. *Geophysical Research Letters*, *37*, L19305. <https://doi.org/10.1029/2010GL044660>
- Finn, C. A., & Morgan, L. A. (2002). High-resolution aeromagnetic mapping of volcanic terrain, Yellowstone National Park. *Journal of Volcanology and Geothermal Research*, *115*(1–2), 207–231. [https://doi.org/10.1016/S0377-0273\(01\)00317-1](https://doi.org/10.1016/S0377-0273(01)00317-1)
- Fournier, R. O. (1989). Geochemistry and dynamics of the Yellowstone National Park hydrothermal system. *Annual Review of Earth and Planetary Sciences*, *17*, 13–53. <https://doi.org/10.1146/annurev.ea.17.050189.000305>
- Fowler, A. P. G., Tan, C., Cino, C., Scheuermann, P., Volk, M. W. R., Shanks, W. C. P., III, & Seyfried, W. E., Jr. (2019a). Vapor-driven sublacustrine vents in Yellowstone Lake, Wyoming, USA. *Geology*, *47*(3), 223–226. <https://doi.org/10.1130/G45577.1>
- Fowler, A. P. G., Tan, C., Luttrell, K., Tudor, A., Scheuermann, P., Pat Shanks, W. C., III, & Seyfried, W. E., Jr. (2019b). Geochemical heterogeneity of sublacustrine hydrothermal vents in Yellowstone Lake, Wyoming. *Journal of Volcanology and Geothermal Research*, *386*, 106677. <https://doi.org/10.1016/j.jvolgeores.2019.106677>
- Hochstein, M. P., & Bromley, C. J. (2005). Measurement of heat flux from steaming ground. *Geothermics*, *34*, 131–158. <https://doi.org/10.1016/j.geothermics.2004.04.002>
- Hurwitz, S., Clor, L. E., McCleskey, R. B., Nordstrom, D. K., Hunt, A. G., & Evans, W. C. (2016). Dissolved gases in hydrothermal (phreatic) and geyser eruptions at Yellowstone National Park, USA. *Geology*, *44*, G37478.1. <https://doi.org/10.1130/g37478.1>
- Hurwitz, S., Harris, R. N., Werner, C. A., & Murphy, F. (2012). Heat flow in vapor dominated areas of the Yellowstone Plateau Volcanic Field: Implications for the thermal budget of the Yellowstone Caldera. *Journal of Geophysical Research*, *117*, B10207. <https://doi.org/10.1029/2012JB009463>
- Hurwitz, S., & Lowenstern, J. B. (2014). Dynamics of the Yellowstone hydrothermal system. *Reviews of Geophysics*, *52*, 375–411. <https://doi.org/10.1002/2014RG000452>
- Ingebritsen, S. E., & Sorey, M. L. (1988). Vapor-dominated zones within hydrothermal systems: Evolution and natural state. *Journal of Geophysical Research*, *93*, 13635–13655. <https://doi.org/10.1029/JB093iB11p13635>
- Johnson, S. Y., Stephenson, W. J., Morgan, L. A., Shanks, W. C., III, & Pierce, K. L. (2003). Hydrothermal and tectonic activity in northern Yellowstone Lake, Wyoming. *Bulletin of the Geological Society of America*, *115*, 954–971. <https://doi.org/10.1130/B25111.1>
- Licciardi, J. M., & Pierce, K. L. (2018). History and dynamics of the greater Yellowstone Glacial system during the last two glaciations. *Quaternary Science Reviews*, *200*, 1–33. <https://doi.org/10.1016/j.quascirev.2018.08.027>
- Lowenstern, J. B., Bergfeld, D., Evans, W. C., & Hurwitz, S. (2012). Generation and evolution of hydrothermal fluids at Yellowstone: Insights from the Heart Lake Geyser Basin. *Geochemistry Geophysics and Geosystems*, *13*, Q01017. <https://doi.org/10.1029/2011GC003835>
- Lowenstern, J. B., & Hurwitz, S. (2008). Monitoring a supervolcano in repose: Heat and volatile flux at the Yellowstone Caldera. *Elements*, *4*, 35–40. <https://doi.org/10.2113/GSELEMENTS.4.1.35>
- Lubimova, E. A., Von Herzen, R. P., & Udintsev, G. B. (1965). On heat transfer through the ocean floor. *Geophysical Monograph Series*, *8*, 78–86. <https://doi.org/10.1029/gm008p0078>
- Luttrell, K., Mencin, D., Francis, O., & Hurwitz, S. (2013). Constraints on the upper crustal magma reservoir beneath Yellowstone Caldera inferred from Lake-Seiche induced strain observations. *Geophysical Research Letters*, *40*, 501–506. <https://doi.org/10.1002/grl.50155>

- Massin, F., Farrell, J., & Smith, R. B. (2013). Repeating earthquakes in the Yellowstone volcanic field: Implications for rupture dynamics, ground deformation, and migration in earthquake swarms. *Journal of Volcanology and Geothermal Research*, 257, 159–173. <https://doi.org/10.1016/j.jvolgeores.2013.03.022>
- McGuinness, M. J., Blakeley, M., Pruess, K., & O'Sullivan, M. J. (1993). Geothermal heat pipe stability: Solution selection by upstreaming and boundary conditions. *Transport in Porous Media*, 11, 71–100. <https://doi.org/10.1007/BF00614636>
- Morgan, L. A., Shanks, W. C., III, Loyalvo, D. A., Johnson, S. Y., Stephenson, W. J., Pierce, K. L., et al. (2003). Exploration and discovery in Yellowstone Lake: Results from high-resolution sonar imaging, seismic reflection profiling, and submersible studies. *Journal of Volcanology and Geothermal Research*, 122, 221–242. [https://doi.org/10.1016/S0377-0273\(02\)00503-6](https://doi.org/10.1016/S0377-0273(02)00503-6)
- Morgan, L. A., Shanks, W. C. P., III, & Pierce, K. L. (2009). Hydrothermal processes above the Yellowstone magma chamber: Large hydrothermal systems and large hydrothermal explosions. *Special Paper of the Geological Society of America*, 459, 1–95. <https://doi.org/10.1130/2009.2459>
- Morgan, P., Blackwell, D. D., Spafford, R. E., & Smith, R. B. (1977). Heat flow measurements in Yellowstone Lake and the thermal structure of the Yellowstone Caldera. *Journal of Geophysical Research*, 82, 3719–3732. <https://doi.org/10.1029/JB082i026p03719>
- Nagihara, S., & Lister, C. R. B. (1993). Accuracy of marine heat-flow instrumentation: Numerical studies on the effects of probe construction and the data reduction scheme. *Geophysical Journal International*, 112, 161–177. <https://doi.org/10.1111/j.1365-246X.1993.tb01447.x>
- Nield, D. A. (1968). The Rayleigh-Jeffreys problem with boundary slab of finite conductivity. *Journal of Fluid Mechanics*, 32, 393–398. <https://doi.org/10.1017/S0022112068000790>
- Nordstrom, D. K., McCleskey, R. B., & Ball, J. W. (2009). Sulfur geochemistry of hydrothermal waters in Yellowstone National Park: IV acid-sulfate waters. *Applied Geochemistry*, 24, 191–207. <https://doi.org/10.1016/j.apgeochem.2008.11.019>
- Otis, R. M., Smith, R. B., & Wold, R. J. (1977). Geophysical surveys of Yellowstone Lake, Wyoming. *Journal of Geophysical Research*, 82, 3705–3717. <https://doi.org/10.1029/JB082i026p03705>
- Pruess, K. (1985). A quantitative model of vapor dominated geothermal reservoirs as heat pipes in fractured porous rocks. *Transactions of the Geothermal Resource Council*, 9, 353–361.
- Pruess, K., & Narasimhan, T. N. (1982). On fluid reserves and the production of superheated steam from fractured, vapor-dominated geothermal reservoirs. *Journal of Geophysical Research*, 87, 9329–9339. <https://doi.org/10.1029/JB087iB11p09329>
- Ramondenc, P., Germanovich, L. N., Von Damm, K. L., & Lowell, R. P. (2006). The first measurements of hydrothermal heat output at 9°50'N, East Pacific Rise. *Earth and Planetary Science Letters*, 245, 487–497. <https://doi.org/10.1016/j.epsl.2006.03.023>
- Robens, C. (2021). *Monte Carlo error propagation*. MATLAB Central File Exchange. <https://doi.org/10.1109/iscas51556.2021.9401134>
- Sarrazin, J., Rodier, P., Tivey, M. K., Singh, H., Schultz, A., & Sarradin, P. M. (2009). A dual sensor device to estimate fluid flow velocity at diffuse hydrothermal vents. *Deep Sea Research Part I: Oceanographic Research Papers*, 56, 2065–2074. <https://doi.org/10.1016/j.dsr.2009.06.008>
- Scott, S. W. (2020). Decompression boiling and natural steam cap formation in high-enthalpy geothermal systems. *Journal of Volcanology and Geothermal Research*, 395, 106765. <https://doi.org/10.1016/j.jvolgeores.2019.106765>
- Shanks, W. C., III, Alt, J. C., & Morgan, L. A. (2007). Geochemistry of sub lacustrine hydrothermal deposits in Yellowstone Lake: Hydrothermal reactions, stable isotope systematics, sinter deposition, and spire growth. In L. A. Morgan (Ed.), *Integrated geoscience studies in the greater Yellowstone area: Volcanic, tectonic, and hydrothermal processes in the Yellowstone geocosystem* (pp. 201–234). U.S. Geological Survey Professional Paper 1717. <https://doi.org/10.3133/pp1717>
- Shanks, W. C., III, Morgan, L. A., Balistrieri, L., & Alt, J. C. (2005). Hydrothermal vent fluids, siliceous hydrothermal deposits, and hydrothermally altered sediments in Yellowstone Lake. In W. P. Innskeep, & T. R. McDermott (Eds.), *Geothermal biology and geochemistry in Yellowstone National Park: Bozeman* (pp. 53–72). Montana: Thermal Biology Institute.
- Smith, R. B., Jordan, M., Steinberger, B., Puskas, C. M., Farrell, J., Waite, G. P., et al. (2009). Geodynamics of the Yellowstone hotspot and mantle plume: Seismic and GPS imaging, kinematics, and mantle flow. *Journal of Volcanology and Geothermal Research*, 188, 26–56. <https://doi.org/10.1016/J.Jvolgeores.2009.08.020>
- Sohn, R. A. (2007). Stochastic analysis of exit fluid temperature records from the active TAG hydrothermal mound (Mid-Atlantic Ridge, 26°N): 1. Modes of variability and implications for subsurface flow. *Journal of Geophysical Research*, 112, B07101. <https://doi.org/10.1029/2006JB004435>
- Sohn, R. A., & Harris, R. N. (2021). Spectral analysis of vertical temperature profile time-series data in Yellowstone Lake sediments. *Water Research*, 57. <https://doi.org/10.1029/2020WR028430>
- Sohn, R. A., Luttrell, K., Shroyer, E., Stranne, C., Harris, R. N., & Favorito, J. E. (2019). Observations and modeling of a hydrothermal plume in Yellowstone Lake. *Geophysical Research Letters*, 46, 6435–6442. <https://doi.org/10.1029/2019GL082523>
- Sohn, R., Harris, R., Linder, C., Luttrell, K., Loyalvo, D., Morgan, L., et al. (2017). Exploring the restless floor of Yellowstone Lake. *Eos*, 98. <https://doi.org/10.1029/2017EO087035>
- Spinelli, G. A., Giambalvo, E., & Fisher, A. T. (2004). Sediment permeability, distribution, and influence on fluxes in oceanic basement. In E. E. Davis, & H. Elderfield (Eds.), *Hydrogeology of the oceanic lithosphere* (pp. 151–188). New York: Cambridge University Press.
- Stein, J. S., & Fisher, A. T. (2001). Multiple scales of hydrothermal circulation in Middle Valley, northern Juan de Fuca Ridge: Physical constraints and geologic models. *Journal of Geophysical Research*, 106, 8563–8580. <https://doi.org/10.1029/2000JB900395>
- Strens, M. R., & Cann, J. R. (1986). A fracture-loop thermal balance model of black smoker circulation. *Tectonophysics*, 122, 307–324. [https://doi.org/10.1016/0040-1951\(86\)90149-6](https://doi.org/10.1016/0040-1951(86)90149-6)
- Tan, C., Cino, C. D., Ding, K., & Seyfried, W. E. (2017). High temperature hydrothermal vent fluids in Yellowstone Lake: Observations and insights from in situ pH and redox measurements. *Journal of Volcanology and Geothermal Research*, 343, 263–270. <https://doi.org/10.1016/j.jvolgeores.2017.07.017>
- Tan, C., Fowler, A. P. G., Tudor, A., & Seyfried, W. E. (2020). Heat and mass transport in sublacustrine vents in Yellowstone Lake, Wyoming: In situ chemical and temperature data documenting a dynamic hydrothermal system. *Journal of Volcanology and Geothermal Research*, 405, 107043. <https://doi.org/10.1016/j.jvolgeores.2020.107043>
- Tiller, C. C. (1995). *Postglacial sediment stratigraphy of large lakes in Greater Yellowstone: Scenarios of tectonic and climatic forcing*. University of Minnesota.
- Villinger, H., & Davis, E. E. (1987). A new reduction algorithm for marine heat flow measurements. *Journal of Geophysical Research*, 92, 12846–12856. <https://doi.org/10.1029/JB092iB12p12846>
- Werner, C., & Brantley, S. (2003). CO₂ emissions from the Yellowstone volcanic system. *Geochemistry Geophysics and Geosystems*, 4, 1061. <https://doi.org/10.1029/2002GC000473>

- Werner, C., Hurwitz, S., Evans, W. C., Lowenstern, J. B., Bergfeld, D., Heasler, H., et al. (2008). Volatile emissions and gas geochemistry of Hot Spring Basin, Yellowstone National Park, USA. *Journal of Volcanology and Geothermal Research*, 178, 751–762. <https://doi.org/10.1016/j.jvolgeores.2008.09.016>
- White, D. E., Muffler, L. J. P., & Truesdell, A. H. (1971). Vapor-dominated hydrothermal systems compared with hot-water systems. *Economic Geology*, 66, 75–97. <https://doi.org/10.2113/gsecongeo.66.1.75>
- Wicks, C. W., Thatcher, W., Dzurisin, D., & Svarc, J. (2006). Uplift, thermal unrest and magma intrusion at Yellowstone Caldera. *Nature*, 440, 72–75. <https://doi.org/10.1038/nature04507>
- Zohdy, A. A. R., Anderson, L. A., & Muffler, L. J. P. (1973). Resistivity, self-potential, and induced-polarization surveys of a vapor-dominated geothermal system. *Geophysics*, 38(6), 1130–1144. <https://doi.org/10.1190/1.1440400>